The crustal structure from the Altai Mountains to the Altyn Tagh fault, northwest China

Youxue Wang,[1,2,3] Walter D. Mooney,[2] Xuecheng Yuan,[4] and Robert G. Coleman[5]

Received 30 March 2001; revised 7 November 2002; accepted 17 March 2003; published 28 June 2003.

[1] We present a new crustal section across northwest China based on a seismic refraction profile and geologic mapping. The 1100-km-long section crosses the southern margin of the Chinese Altai Mountains, Junggar Accretional Belt and eastern Junggar basin, easternmost Tianshan Mountains, and easternmost Tarim basin. The crustal velocity structure and Poisson's ratio (σ), which provide a constraint on crustal composition, were determined from *P* and *S* wave data. Despite the complex geology, the crustal thickness along the entire profile is nearly uniform at 50 km. The thickest crust (56 km) occurs at the northern end of the profile beneath the Altai Mountains and the thinnest (46 km) crust is beneath the Junggar basin. Beneath surficial sediments, the crust is found to have three layers with *P* wave velocities (V_p) of 6.0–6.3, 6.3–6.6, and 6.9–7.0 km/s, respectively. The southern half of the profile, including the eastern Tianshan Mountains and eastern margin of the Tarim basin, shows low *P* wave velocities and $\sigma = 0.25$ to a depth of 30 km, which suggests a quartz-rich, granitic upper crustal composition. The northern half of the profile below the Altai Mountains and Junggar Accretional Belt has a higher Poisson's ratio of $\sigma = 0.26–0.27$ to a depth of 30 km, indicative of an intermediate crustal composition. The entire 1100-km-long profile is underlain by a 15–30 km thick high velocity (6.9–7.0 km/s; $\sigma = 0.26–0.28$) lower-crustal layer that we interpret to have a bulk composition of mafic granulite. At the southern end of the profile, a 5-km-thick midcrustal low-velocity layer ($V_p = 5.9$ km/s, $\sigma = 0.25$) underlies the Tianshan and the region to the south, and may be indicative of a near-horizontal detachment interface. P_n velocities are $\sim$7.7–7.8 km/s between the Tianshan and the Junggar basin, and $\sim$7.9–8.0 km/s below the Altai Mountains and eastern margin of the Tarim basin. We interpret the consistent three-layer stratification of the crust to indicate that the crust has undergone partial melting and differentiation after Paleozoic terrane accretion. The thickness (50 km) of the crust appears to be related to compression resulting from the Indo-Asian collision. *INDEX TERMS:* 7205 Seismology: Continental crust (1242); 7218 Seismology: Lithosphere and upper mantle; 8110 Tectonophysics: Continental tectonics—general (0905); *KEYWORDS:* crustal structure, China, seismic refraction, compression, Indo-Asian collision

Citation: Wang, Y., W. D. Mooney, X. Yuan, and R. G. Coleman, The crustal structure from the Altai Mountains to the Altyn Tagh fault, northwest China, *J. Geophys. Res.*, *108*(B6), 2322, doi:10.1029/2001JB000552, 2003.

1. Introduction

[2] Northwest China consists of a 2000-km-wide orogenic belt located between the Siberian craton and the northern edge of the Tibetan plateau. The Indo-Asian collision is the latest in a series of tectonic events that have built this impressive orogenic belt. This region offers excellent field exposures that document a wide range of geological processes that have formed and modified the Earth's crust. Northwest China is considered a "type locality" for studies of crustal accretion, deformation, and stabilization [*Yang and Yang*, 1981; *Zhang et al.*, 1984; *Ren et al.*, 1987; *Yuan et al.*, 1992; *Avouac and Tapponnier*, 1993; *Dong*, 1993; *Berzin et al.*, 1994; *Rowly*, 1996; *Yin and Nie*, 1996].

[3] As part of a geoscience transect that extended from the Altai Mountains to Taiwan, a 1100-km-long seismic refraction survey was conducted across northwest China (Figures 1 and 2) by the former Ministry of Geology and Mineral Resources (MGMR). The three-component seismic data were acquired in 1988. The goal of this project was to gain a better understanding of the deep crustal structure beneath different tectonic provinces in the area and to provide crustal information for mineral resources development [*Xu and Wang*, 1991; *Wang*, 1992; *Yuan et al.*, 1992].

[4] Prior information regarding the seismic properties of the crust and upper mantle in northwest China have been obtained using local and teleseismic tomography [*Liu et al.*,

[1]China University of Geoscience, Beijing, China.
[2]U.S. Geological Survey, Menlo Park, California, USA.
[3]Now at Department of Resources and Environmental Engineering, Guilin Institute of Technology, Guilin, China.
[4]China Geological Survey, Beijing, China.
[5]Department of Geology and Environmental Sciences, Stanford University, Stanford, California, USA.

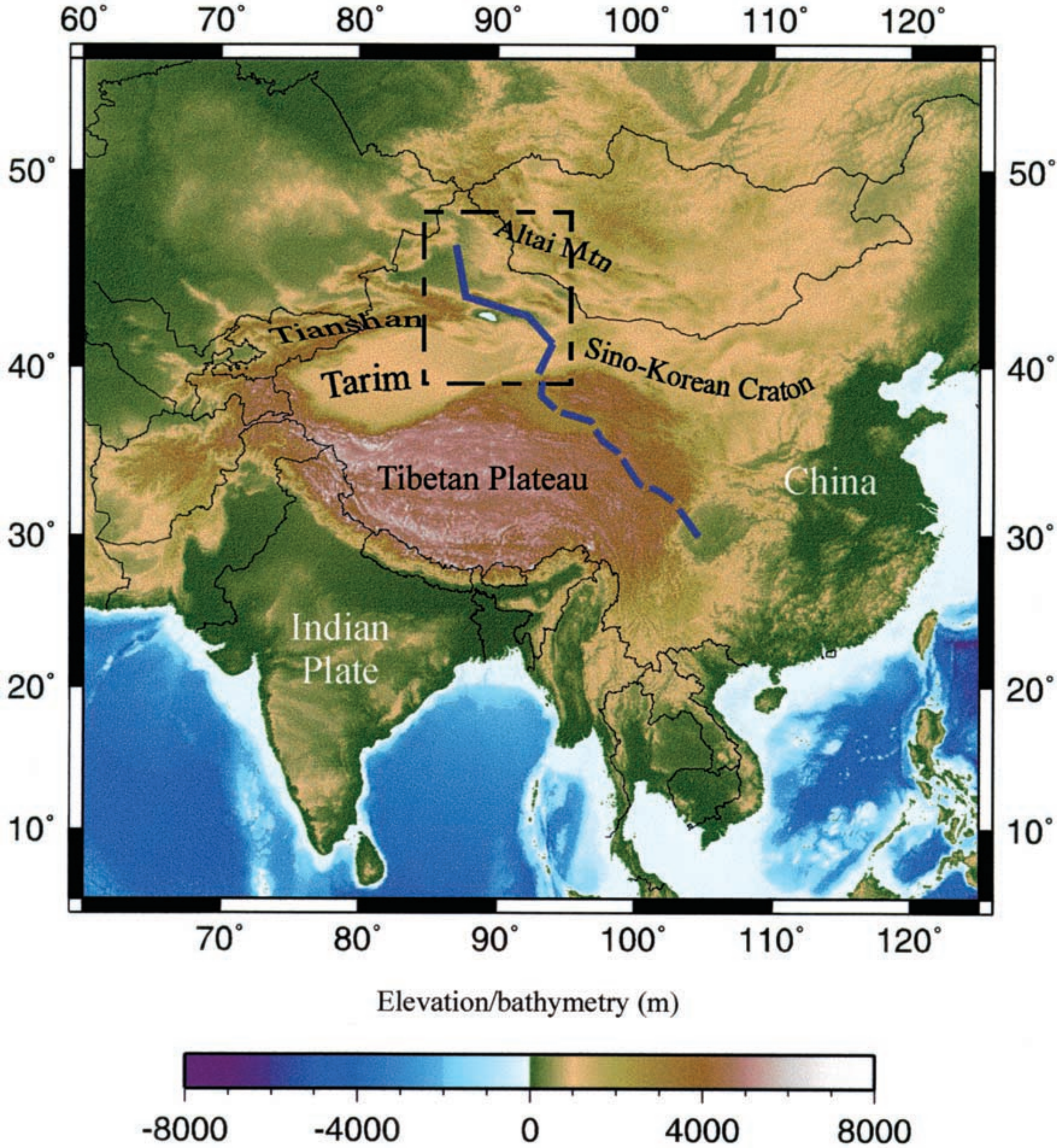

Figure 1. Topographic relief map of southeast Asia with seismic transect indicated by a heavy dark line. The entire transect is located north of the Tibetan Plateau, and crosses from the Altai Mountains to the eastern Tarim basin. The transect is composed of four linear segments. The box indicates the area depicted in Figure 2. The dashed line across the eastern Tibetan Plateau is the southward continuation of the seismic transect reported here.

1989; *Roecker et al.*, 1993; *Teng et al.*, 1992, 1994], the analysis of seismic surface waves [*Feng et al.*, 1980; *Cotton and Avouac*, 1994; *Mahdi and Pavlis*, 1998], seismic refraction studies in the southwestern Tarim basin [*Kao et al.*, 2001], and modeling of gravity data [*Burov et al.*, 1990]. The majority of prior work has focused on the region of the Tianshan where a crustal thickness of 50–55 km has been reported [*Roecker et al.*, 1993]. Prior work has not included the crustal structure of the Altai Mountains or the eastern edge of the Tarim basin, as we present here. *Cotton and Avouac* [1994] report low shear wave velocities in our study area, a result that is consistent with our observations. There have been geophysical studies of the Junngar basin, but these have mainly addressed shallow depths where hydrocarbon deposits are known [e.g., *Song et al.*, 2000] and these data have not been made available.

[5] This information, combined with recent advances in processing techniques of three-component data, have enabled us to model both the *P* and *S* wave velocity structure (V_p and V_s, respectively), and to infer compositional changes within the crust and uppermost mantle using Poisson's ratio [*Castagna*, 1985; *Holbrook et al.*, 1988, 1992; *Eesley*, 1989; *Gajewski et al.*, 1990; *Romero et al.*, 1993; *Zandt et al.*, 1994; *Kosminskaya*, 1995; *Krilov et al.*, 1995; *Christensen and Mooney*, 1995; *Christensen*, 1996; *Catchings and Lee*, 1996; *Hawman*, 1996; *Kern et al.*, 1999; *Swenson et al.*,

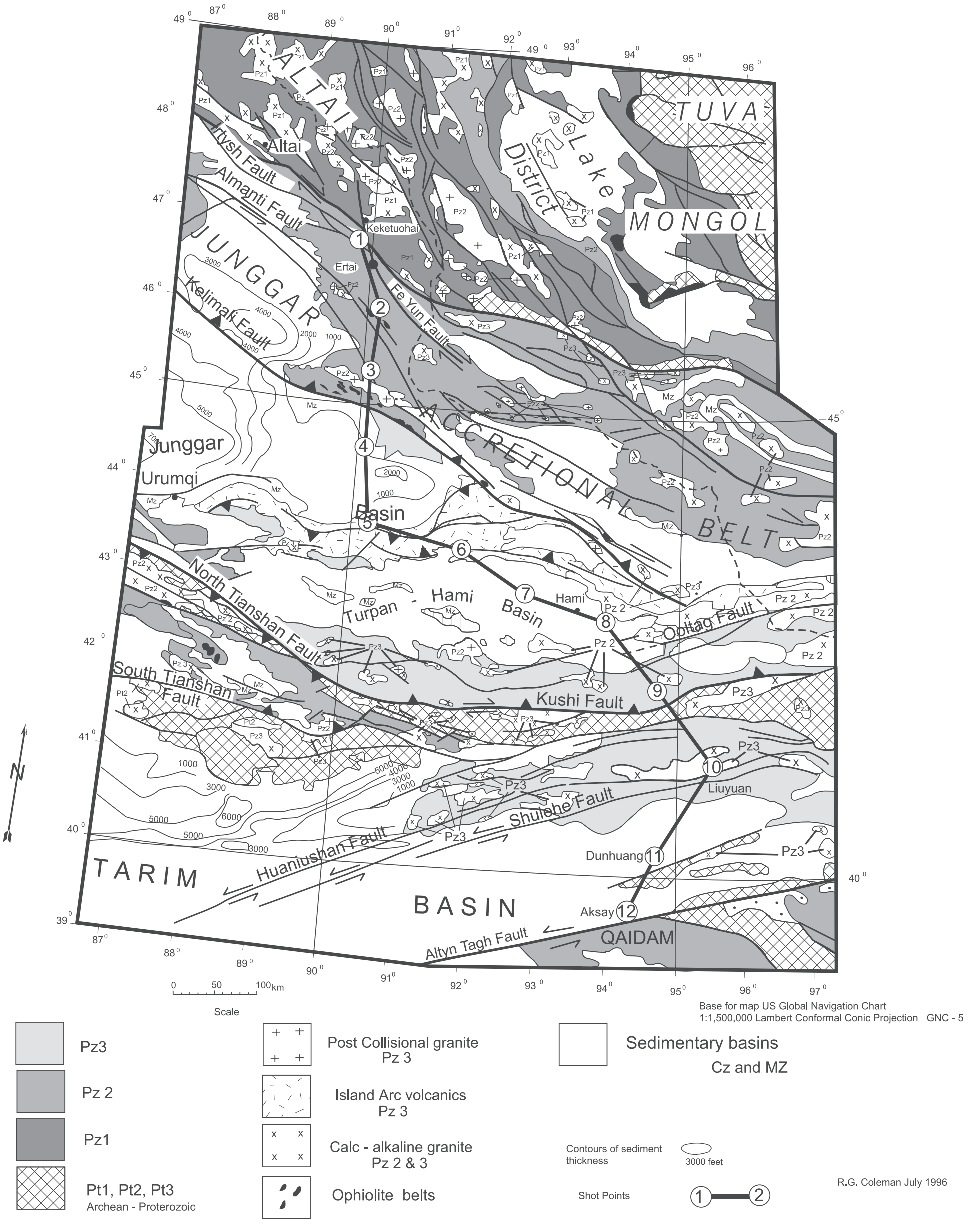

Figure 2. Geological map of the region investigated by the seismic transect. The transect location is indicated by a solid line; circled numbers 1 through 12 indicate shot point locations. The northernmost shot point (SP1) is located at the boundary between the Altai Mountains and the Junggar Accretional Belt. The southernmost shot point (SP12) is located adjacent to the Altyn Tagh fault. The seismic transect crosses, in addition, the eastern Junggar basin, Bogda Shan arc (SP5-6), the Turpan-Hami basin (SP6-9), the Tienshan (SP9-10), and the eastern Tarim basin (SP10-12).

2000]. In this paper we present the *P* and *S* wave velocity structure of the crust from our seismic refraction data, and describe an interpretive geological crustal section that is based on these results and geologic mapping.

2. Geological Setting

[6] Southern Eurasia, of which northwestern China is a part, was formed by the coalescence and accretion of diverse crustal fragments from a series of collisional events during Paleozoic and Mesozoic times [*Yang and Yang*, 1981; *Zhang et al.*, 1984; *Ren et al.*, 1987; *Zhang*, 1997; *Berzin et al.*, 1994; *Carroll et al.*, 1995; *Rowly*, 1996; *Yin and Nie*, 1996; *Neil and Houseman*, 1997; *Yin et al.*, 1998]. Most of western China, including the Altai Mountains, Junggar basin, Tianshan Mountains (henceforth simply the Tianshan, since ''shan'' means ''mountains''), and the eastern margin of the Tarim basin (Figure 2), where assembled prior to the mid-Cenozoic Indo-Asian collision that reshaped the region and reactivated older structures [*Molnar and Tapponnier*, 1975; *Tao and Lu*, 1981; *Tapponnier et al.*, 1982, 2001; *Windley et al.*, 1990; *Dong*, 1993; *Avouac and Tapponnier*, 1993; *Avouac et al.*, 1993; *Liu et al.*, 1994; *Allen et al.*, 1995; *Yin and Nie*, 1996].

[7] The tectonic terranes comprising the study area are bounded by faults and inferred sutures (Figure 2). Some of

these faults are seismically active and have been sites of major historic earthquakes, while others are aseismic and mark the sutures between Paleozoic and Mesozoic terranes. The geologic makeup and tectonic history of each separate terrane is briefly discussed from north to south.

2.1. The South Margin of the Altai Mountains and the Junggar Fold (Accretional) Belt

[8] The Altai Mountains (north of shot point 1, Figure 2) includes a 12-km-thick early Paleozoic accretionary wedge, consisting of metamorphosed sandstone, shales, and minor limestones. Intercalated within these sedimentary sequences are mid-Paleozoic island arc volcanics and calc-alkaline intrusives [*Sengor et al.*, 1993; *Qu and He*, 1993; *Cunningham et al.*, 1996a, 1996b]. Gneissic rocks along the southern border are believed to comprise the Precambrian basement [*Feng et al.*, 1989], but the existence of older basement in the Altai is not yet resolved. *Windley et al.* [1994] suggest that these gneisses may represent Precambrian to early Paleozoic accreted fragments. This suggestion is supported by *Berzin et al.* [1994] who show the Altai Mountains as a microcontinent with possible Precambrian basement [*Bibkova et al.*, 1992].

[9] The Junggar Accretional Belt (shot points 1, 2, and 3; Figure 2) is bound by the Irtysh and Kelimali faults and consists mainly of accreted Devonian and Carboniferous sediments and volcanics with a few scattered Ordovician and Silurian rocks [*Feng et al.*, 1980], and is a part of the south margin of the Altai Block. Dismembered ophiolites and associated cherts that record the involvement of oceanic crust of the Paleo-Junggar Ocean in the accretion process are concentrated along the Irtysh, Kelimali, and Almanti faults (Figure 2). The ages of these rocks indicate continued subduction and accretion from the Middle Devonian to the Early Carboniferous. Within the Altai and Junggar Mountains, Paleozoic calc-alkaline intrusions were formed above a northward-dipping oceanic slab. The Paleozoic calc-alkaline plutons predate the final Late Carboniferous to Early Permian amalgamation along the North and central Tianshan suture.

2.2. The Junggar Basin

[10] The sediments of the Junggar basin (shot points 4 and 5; Figure 2) have been deposited on a basement similar to that of the Junggar Accretionary Belt [*Feng et al.*, 1980; *Tao and Lu*, 1981; *Kwon et al.*, 1989; *Carroll et al.*, 1990, 1995; *Allen et al.*, 1991, 1995]. The basin is triangular in shape and filled with deposits thickening gradually from north to south, and the largest accumulations being found along the Bogda Shan island arc (Figure 2). The basal Upper Permian deposits of the Junggar basin are nonmarine and were deposited within the subsiding foreland basin [*Kwon et al.*, 1989; *Carroll et al.*, 1990]. Geological reconstructions suggest that the basement underlying the Junggar basin consists of incompletely subducted, imbricated mid-Carboniferous oceanic crust and trench-wedge volcanoclastic sediment.

2.3. The Bogda Shan Volcanic Arc

[11] The Carboniferous Bogda Shan volcanic arc, south of the Junggar basin (shot points 5 and 6; Figure 2), was formed as a consequence of northward subduction and extension during and prior to the accretion of the Paleozoic and Precambrian Tianshan blocks. The arc appears to be centered in the Bogda Shan where thick sections of Carboniferous submarine pyroclastics and basalt-andesite flows extend north and south across the present Junggar and Turpan basins [*Coleman*, 1989] (Figure 2). To the west of the Bogda Shan, the Carboniferous volcanics rest unconformably on an early Paleozoic accretionary complex of trench sediment and dismembered ophiolite. Evidence for a Precambrian basement underlying these Carboniferous volcanics is not seen along the northern front of the Bogda Shan [*Ren et al.*, 1987]. Similar Permian lacustrine deposits and overlying felsic clastics in both basins suggest that an Andean-type arc did not separate the Turpan and Junggar basins at this time [*Greene et al.*, 1997].

2.4. The Turpan-Hami Basin

[12] The depositional sequences in the Turpan-Hami basin (shot points 7, 8, and 9; Figure 2) are similar to those in the Junggar basin and consist of basal Carboniferous andesitic volcanics, overlain by Permian lacustrine mudstones interlayered with continental fluvial and volcanic sediments. The Permian sequence is overlain by nearly 3000 m of Triassic and Jurassic foreland-style continental deposits, rich in coals and lacustrine mudstones [*Carroll et al.*, 1995; *Greene et al.*, 1997]. The Carboniferous volcanoclastic sequences exposed on the southern margins of the Turpan-Hami basin are intruded by late Paleozoic calc-alkaline granites related to the Bogda Shan arc.

2.5. The Tianshan

[13] Located south of the Kushi fault (shot point 10; Figure 2) (also called the South Tianshan fault or Nicolaev Line), the Tianshan has been tightly compressed during Mesozoic and Cenozoic time. The central Tianshan consists of Proterozoic gneiss and schist intruded by Paleozoic calc-alkaline granite [*Allen et al.*, 1992, 1993; *Windley et al.*, 1990]. These older rocks are overlain by passive margin carbonate and continental clastics of Middle and Upper Proterozoic age [*Ren et al.*, 1987]. The rock formations of the South Tianshan merge with the passive margin of the Tarim Platform. A late Paleozoic subduction scenario between the Tarim and central Tianshan has been suggested by *Allen et al.* [1992] based on fragments of ophiolite bodies found within the South Tianshan fault zone. Further east, the central Tianshan wedges out as a result of dextral strike-slip faulting and crustal subduction of the central Tianshan block under the north-facing passive margin of the Tarim Platform (Figure 1). Finally, the Cenozoic shortening of this area is considered to result from the collision of the Indian Craton to the south [*Carroll et al.*, 1995; *Windley et al.*, 1994; *Hendrix et al.*, 1994]. The Cenozoic imbrication, and thickening of the crustal section south of the Bogda Shan, was accomplished by thrusting and strike-slip faulting at the surface, submerging the central Tianshan under the Tarim passive margin (Figure 2). Present-day strike-slip motion along the Altyn Tagh (Figure 2) and thrusting in the area [*Zhou and Graham*, 1996] has, together with convergence, produced an unusually thick (50 km) continental crust beneath the seismic transect at this location.

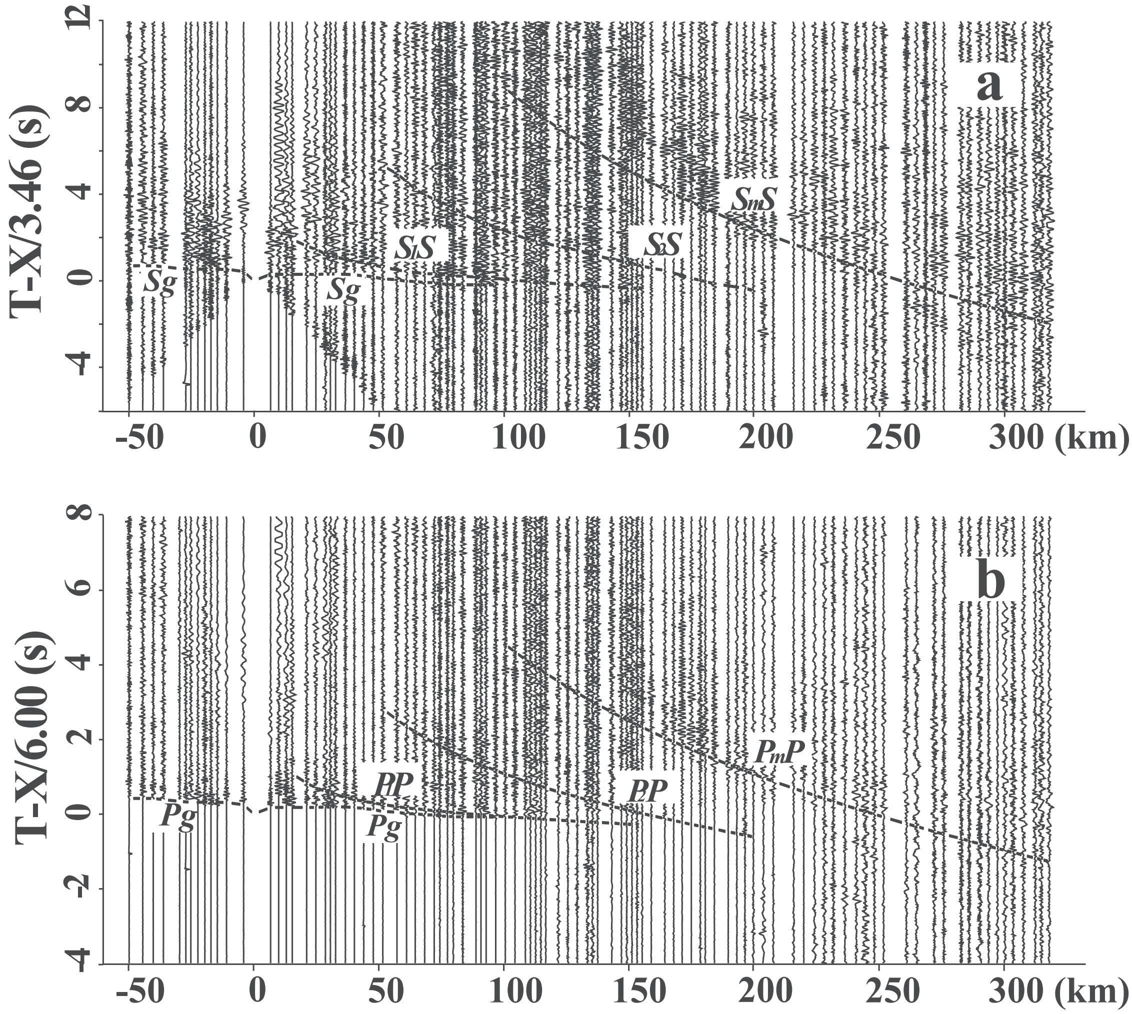

Figure 3. Record sections of shot point SP1. (a) Trace-normalized band-pass filtered (0–8 Hz) *S* wave record section with a reduction velocity of 3.46 km/s and a factor of 0.58 in timescale with respect to *P* wave record section; (b) trace-normalized *P* wave record section with a reduction velocity of 6.00 km/s. The wide-angle reflection from the Moho (P_mP) is delayed by the thick (56 km) crust of the Altai Mountains.

2.6. The Tarim Basin

[14] The Tarim basin (shot points 11 and 12; Figure 2) is filled with a thick (~6 km along our profile) foreland sequence of Mesozoic and Cenozoic continental sediments. These are underlain by Paleozoic shallow marine sediments, and Late Proterozoic rocks which floor the entire basin [*Jia et al.*, 1991; *Allen et al.*, 1991; *Sobel*, 1999]. The Altyn Tagh fault system has exposed possible Archean basement on the southern boundary of this craton. These inferred older rocks are intruded by early Paleozoic calc-alkaline granite (Figure 2).

2.7. The Altyn Tagh Fault and the Qaidam Depression

[15] The Altyn Tagh fault zone (shot point 12; Figure 2) truncates the E-W trending Qaidam units, juxtaposing them against the mildly deformed Tarim Platform sequences [*Zhou and Graham*, 1996; *Ritts and Biffi*, 2000]. The Qaidam Depression is filled with Mesozoic to Cenozoic basinal sequences of lacustrine and fluvial fan deposits [*Carroll et al.*, 1990; *Ritts*, 1995]. The basement consists of a late Paleozoic fold belt containing active continental-margin sediments and volcanics. The entire sequence is strongly folded and is related to the E-W trending Kunlun suture which shows evidence of Paleozoic convergence with its high-pressure/low-temperature metamorphic rocks [*Chen et al.*, 1999].

3. Seismic Data

3.1. Acquisition and Processing

[16] Seismic energy was provided by 12 chemical explosive shots fired in boreholes. The charge size ranged from 1500 to 4000 kg, sufficient to provide clear first arrivals to a maximum distance of 300 km. The distance between shot points ranged from 63 to 125 km, and the interval between portable seismographs was between 2 and 4 km. The profile was recorded along existing roads and provided four nearly straight profile segments (Figure 2).

[17] To assist in phase correlation, record sections with reduction velocities of 6.0 and 3.46 km/s were used for *P* and *S* waves, respectively. The timescale used for *S* wave record sections was compressed by a factor of 0.58 in order

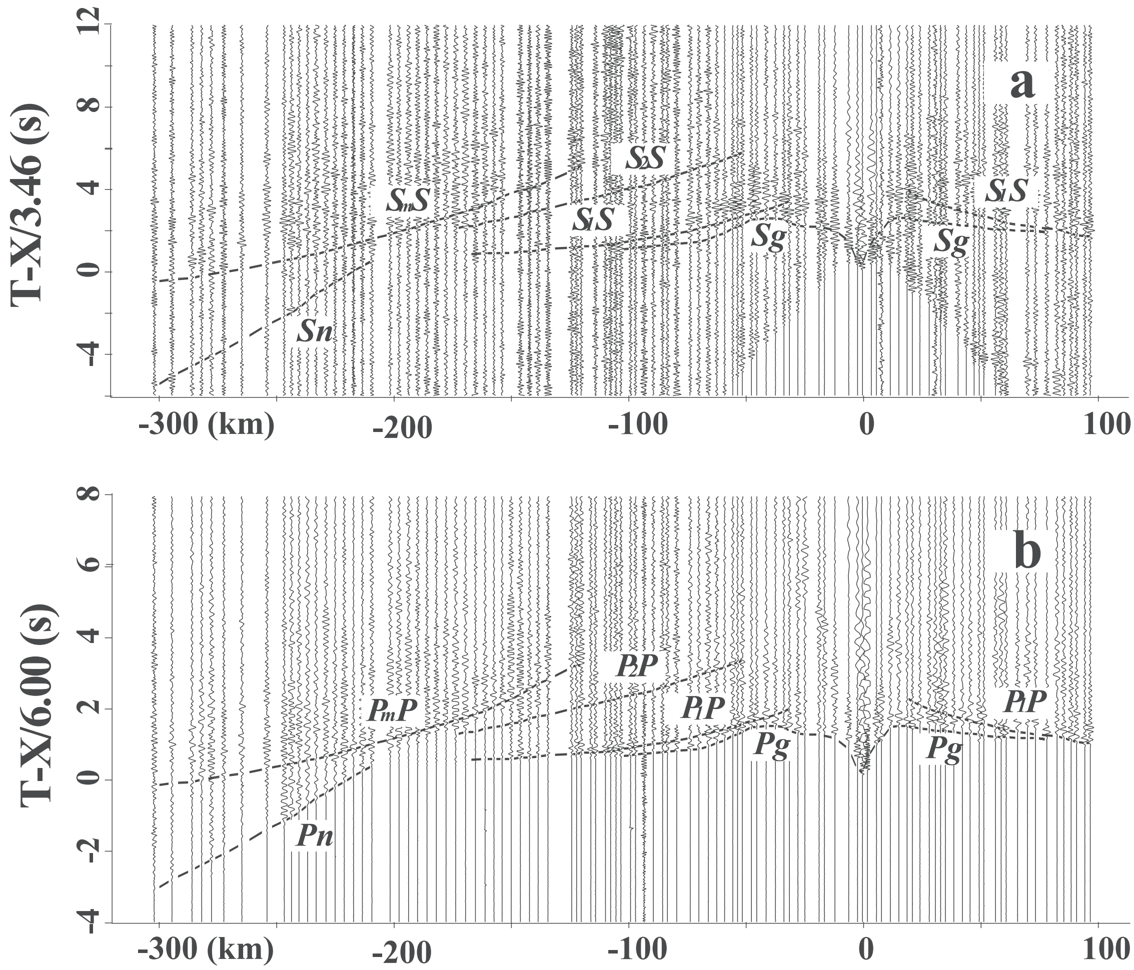

Figure 4. Record sections of shot point SP4. (a) Trace-normalized band-pass filtered (0–8 Hz) *S* wave record section (transverse component) with a reduction velocity of 3.46 km/s and a factor of 0.58 in timescale with respect to *P* wave record section; (b) trace-normalized *P* wave record section with a reduction velocity of 6.00 km/s. The wide-angle reflection from the Moho (P_mP) and the refracted arrival from below the Moho (P_n) are very clear on the *P* wave record section.

to match the *P* wave arrival times. To avoid the small time shift introduced by digital filters, unfiltered *P* wave data were used for phase correlation and travel time picking. In order to improve the signal-to-noise ratio for phase correlation, the *S* wave data were filtered with a 0–8 Hz band pass.

3.2. Correlation of Phases

[18] Standard nomenclature has been used to identify first and secondary arrival phases. The upper crustal refraction commonly referred to as P_g and S_g actually corresponds to two travel time segments (Figures 3 and 4). The first, usually a short travel time branch that propagates very near the shot point, is a diving wave within the sedimentary layer, whereas the second and much longer travel time branch is the refraction (or diving wave) from the top of basement. True first-arrival refractions from the middle or lower crust were rarely observed. Much more apparent were wide-angle reflections, that are labeled P_1P and S_1S, P_2P and S_2S, and P_LP and S_LS, corresponding to reflections from the top of the middle crust, lower crust, and low-velocity layer (where present) for *P* and *S* waves, respectively. The phase P_mP (S_mS) is the reflection from the Moho, and P_n (S_n) is the refraction from the Moho.

[19] In general, P_g is a very clear phase that contains detailed information about the upper crustal velocity structure. The S_g phase is not always as clear as P_g because of a lower signal-to-noise ratio. The first segment of P_g (S_g) corresponds to waves propagating in the sediments or weathered layer, and is the first arrival within a distance of 50 km of the shot points. *P* wave velocities observed within the three basins that are crossed (Figure 2) indicate a higher velocity gradient than is measured within the crystalline crust. The apparent velocities for P_g and S_g from shot points SP4 (Figure 4) and SP7 (Figure 5), which are located in the Junggar and Turpan basins, respectively, are relatively low (<5.00 km/s for *P* wave and <2.60 km/s for *S* wave) corresponding to thick sediments. Where sediments are absent, the velocities of P_g and S_g are about 6.0 and 3.46 km/s, respectively (Figures 3 and 6).

[20] The phase that arrives after P_g (S_g) is the wide-angle reflection P_1P (S_1S) from the top of the middle crust (6.3–6.6 km/s). At certain distances, P_1P seems to be a first arrival because the P_g energy is too weak to be detected.

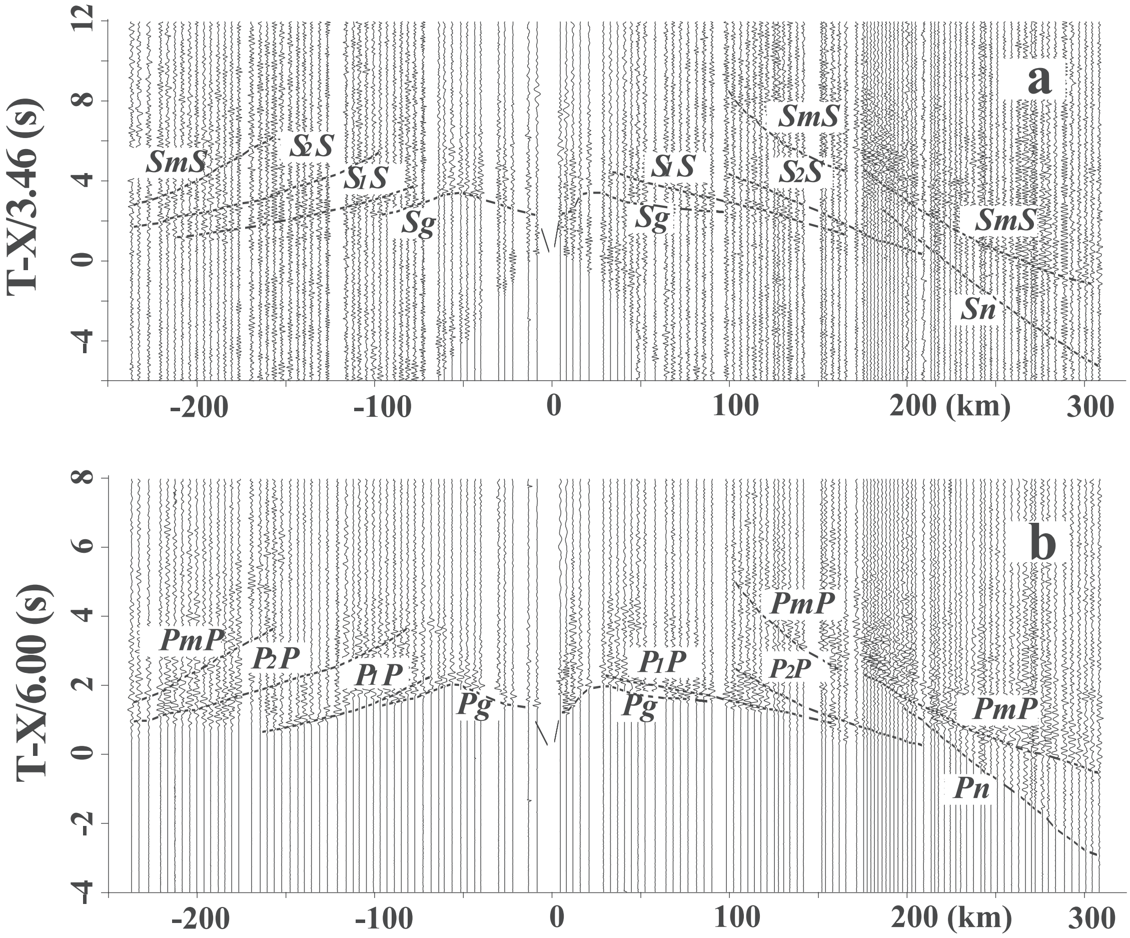

Figure 5. Record sections of shot point SP7. (a) Trace-normalized band-pass filtered (0–8 Hz) S wave record section with a reduction velocity of 3.46 km/s and a factor of 0.58 in timescale with respect to P wave record section; (b) trace-normalized P wave record section with a reduction velocity of 6.0 km/s. Intracrustal wide-angle reflections, the reflection from Moho (P_mP), and the refraction from below Moho are all clearly recorded.

The phase P_2P (S_2S) corresponds to a reflection from the top of the lower crust (6.8–7.0 km/s), and is visible on many of the record sections. P_2P (S_2S) intersects P_mP (S_mS) (the Moho reflection) at a distance of 200–250 km from the shot. Despite the dominance of the P_mP (S_mS) phase, the P_2P (S_2S) phase can often be clearly identified.

[21] To the south of shot point SP8 (Figure 2), another phase, referred to as P_LP (S_LS) (Figure 6), can be identified just above the signal-to-noise level in the record sections between P_1P (S_1S) and P_2P (S_2S). Despite its weak energy, this phase is visible in the trace-normalized record section when compared to the very strong P_mP (S_mS) phase (Figure 6). P_LP (S_LS) nearly parallels P_1P (S_1S), but has a lower average velocity. It is the low-velocity zone (LVZ) that gives rise to this phase that delays the Moho reflections in the related regions (Figures 5 and 6). No obvious time delay appears for the phases before P_2P (S_2S), and therefore the phase P_LP (S_LS) is interpreted to be a reflection from the top of a low-velocity layer beneath the southern section of the profile (Tianshan, Turpan-Hami basin, and eastern Tarim basin).

[22] The Moho reflection P_mP (S_mS) is the dominant phase on all record sections at distances greater than 100–150 km. Due to the existence of a complex crustal structure, especially the midcrustal low-velocity layer below the southern part of the profile, the phase P_mP (S_mS) sometimes exists in two segments with a clear time delay separating them. Examples of this phenomenon can be found in the record sections from shot points SP7 (Figure 5) and SP10 (Figure 6). In the record section of SP7, the arrivals of P_mP (S_mS) reflections arrive later at a distance greater than 170 km. Likewise for SP10, the travel times of P_mP and S_mS are delayed at distances less than about 200 km from the shot in the northern segment. These results indicate that the northern limit of the deep crustal low-velocity layer must be located somewhere between SP8 and SP9 along the profile near the northern edge of the Tianshan (Figure 2).

[23] P_n was observed as the first arrival in several record sections at distances greater than 200 km (Figures 4–6). The apparent velocity of P_n ranges from 7.6 to 7.9 km/s. The lowest values occur beneath the Junggar and Turpan-Hami basins, but P_n has a high apparent velocity beneath the Altai Mountains, Junggar Accretional Belt, Tianshan Accretional Belt, and eastern margin of the Tarim platform. S_n is also visible in some S wave sections. Forward

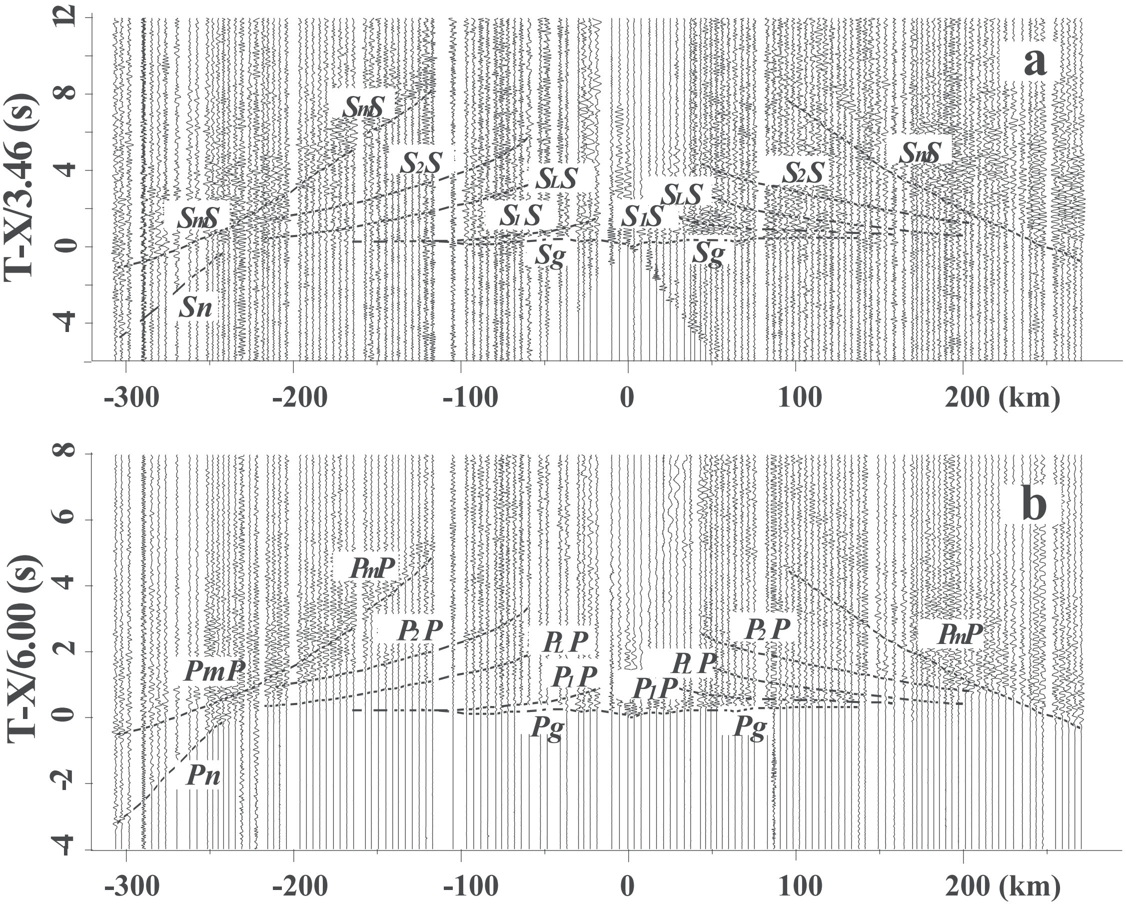

Figure 6. Record sections of shot point SP10. (a) Trace-normalized band-pass filtered (0–8 Hz) *S* wave record section with a reduction velocity of 3.46 km/s and a factor of 0.58 in timescale with respect to *P* wave record section; (b) trace-normalized *P* wave record section with a reduction velocity of 6.0 km/s. The *S* wave record section shows a very clear wide-angle reflection from the Moho, as well as clear *P* wave and *S* wave refracted arrivals from below Moho.

modeling of P_n observations was used to determine the velocity structure of the uppermost mantle.

4. Modeling the Data

[24] Using the abovementioned phase correlations, the first arrivals of P_g were used to invert for the upper crustal velocity structure using a finite difference tomographic method [*Kelly et al.*, 1976; *Hole*, 1992; *Ohminato and Chouet*, 1997]. The reflection phases P_1P, P_LP, P_2P, and P_mP were used to determine the approximate velocity structure of the middle to lower crust using a combination of the x^2-t^2 method [*Giese et al.*, 1976] and the reflectivity method [*Fuchs and Müller*, 1971]. After establishing an initial crustal *P* wave velocity structure, the final *P* wave model was determined using 2-D forward raytracing [*Cerveny et al.*, 1977; *Cerveny and Psencik*, 1984]. Travel times and amplitudes of the various phases on the record sections were fitted by adjusting the velocities and depths of the boundaries with the raytracing method (Figures 7 and 8), thus establishing the final *P* wave velocity model. The ray method that we have used to model the data is biased toward relatively flat-laying structures with discrete seismic discontinuities. We admit the possibility of alternate seismic models with gradational velocity boundaries rather than first-order discontinuities. However, the main conclusions of this paper would not change significantly if such models were obtained.

[25] In recent years, there has been an increased interest in modeling both the *P* and *S* wave velocity structure of the crust because this combination provides better constraints on composition [e.g., *Castagna*, 1985; *Holbrook et al.*, 1988, 1992; *Eesley*, 1989; *Gajewski et al.*, 1990; *Kosminskaya*, 1995; *Rudnick and Fountain*, 1995; *Zandt and Ammon*, 1995; *Krilov et al.*, 1995; *Hauksson and Haae*, 1997; *Musacchio et al.*, 1997; *Eberhart-Phillips and Michael*, 1998; *Menke et al.*, 1998; *Stoerzel and Simithson*, 1998; *Catchings*, 1999]. We have modeled the *S* wave data by assuming the depths to all boundaries are those obtained from the *P* waves. We were able to fit the travel times for the crystalline upper crust by replacing the *P* wave velocities with *S* wave velocities assuming a Poisson's ratio of 0.25 in the initial *S* wave model. Two-dimensional forward modeling was then used to fit the *S* wave reflections and create a complete *S* wave model for the crust.

[26] Uncertainties in the final velocity model primarily depend on the correct identification of the various phases and the density of rays, the shot point interval, the receiver

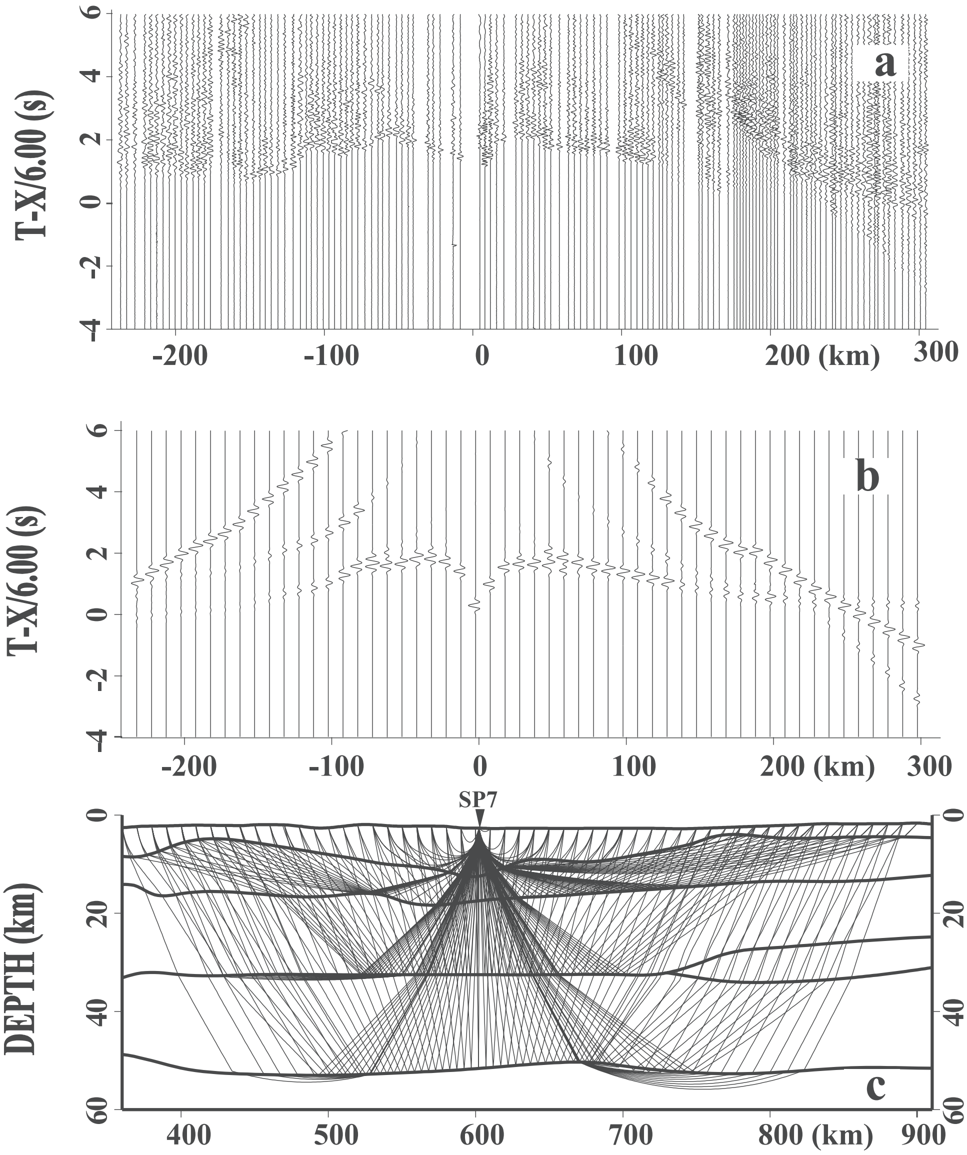

Figure 7. Observed and synthetic record sections of P wave and ray coverage for shot SP7. The wide-angle reflection from the Moho is very clear, as is the refracted arrival from below the Moho (P_n).

density, and the degree of lateral variations in the thickness of surficial sediments. Our result has shown that, depending on the uniformity of the structure and the density of the rays, the ability to resolve velocity and depths to the interfaces are 2 and 5%, respectively (Table 1). Thus a velocity of 7.0 km/s has an uncertainty of ±0.14 km/s and a layer depth of 30 km has an uncertainty of ±1.5 km. The V_p/V_s ratio has an uncertainty of 4%. Figure 9 shows a three-dimensional perspective of the final structural model along the seismic refraction profile. P wave velocity and Poisson's ratio are indicated in this figure.

4.1. Crustal Seismic Velocity Structure

[27] The crustal model (Figures 9 and 10, and Table 1) shows many significant features. As expected, the Junggar, Turpan-Hami, and Tarim sedimentary basins have low velocities and steep velocity gradients with V_p = 3.6–5.8 km/s and V_s = 2.3–3.3 km/s. The Turpan-Hami basin has the greatest thickness (10 km) of sediments. Beneath the eastern Tarim basin, the velocity increases from 4.4 km/s near the surface (V_s = 2.7 km/s) to 5.8 km/s (V_s = 3.3 km/s) at a depth of ~6 km. The strong velocity contrast between the basin fill and the crystalline basement clearly outlines the 2-D configuration of the sedimentary basins. Along most of the profile, the velocity of the crystalline upper crust is 6.0–6.1 km/s at depths 8–14 km. The Bogda Shan, however, is underlain by a higher-velocity block (V_p = 6.30 km/s, V_s = 3.7 km/s) at the same depth range.

[28] A remarkable feature of the crustal model is that the middle crust has a nearly uniform 16 km thickness to the north of the Tianshan despite the complex surface geology. However, the southward-decreasing average seismic velocities in this layer, with a LVZ, indicates a nonuniform composition. From the Altai block to the Turpan-Hami basin, middle-crustal velocities are 6.5–6.6 km/s. Further south, beneath the Tianshan, Tarim basin, and Qaidam basin, the velocity drops to 6.3 km/s, and a 5-km-thick LVZ with an estimated P wave velocity of 5.9 km/s is

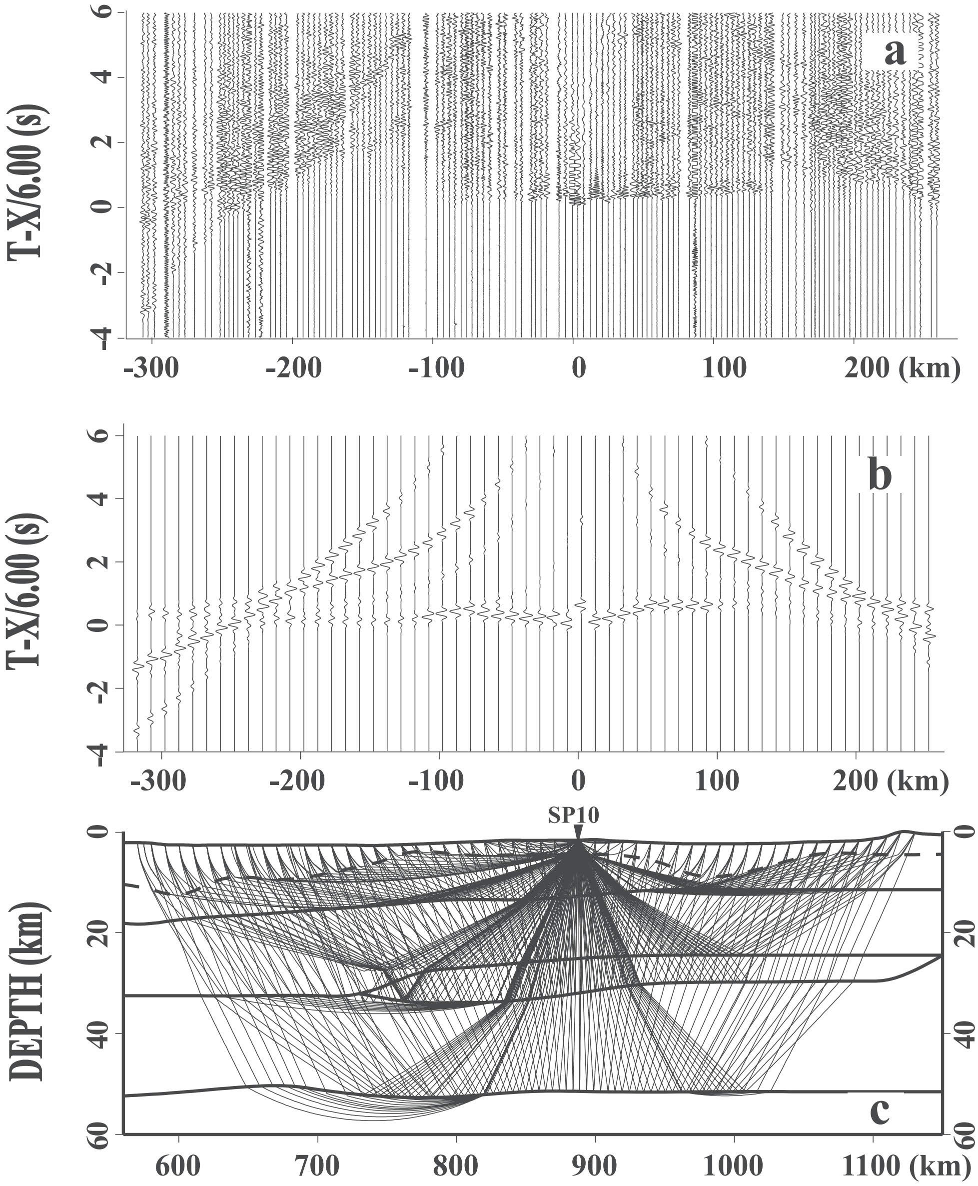

Figure 8. Observed and synthetic record sections of P wave and ray coverage for shot SP10. Wide-angle reflections are clearly observed, as is the refracted arrival from below the Moho (P_n).

located at ~25 km depth. The LVZ causes clearly observed time delays of the Moho reflections recorded south of Tianshan (Figures 5–8).

[29] The entire seismic profile is underlain by a remarkably uniform high-velocity (6.9–7.0 km/s) lower crust whose top is at a depth of 25–30 km. The lower crust has an average thickness of about 20 km. The maximum lower crustal thickness (30 km) is found to the north, beneath the Altai Mountains, where the Moho is at a maximum depth of 55 km (Figure 9). The thickening of the lower crust is accommodated by both deepening of the Moho and thinning (isostatic uplift) of the upper crust. The thinnest (15 km) portion of the lower crust underlies the Junggar basin, where the Moho depth is 46 km. South of the Junggar basin, the Moho depth increases to about 50 km and then deepens abruptly (to about 68 km) to the south of the Altyn Tagh fault [*Wang et al.*, 1997].

[30] The seismic velocity of the uppermost mantle (P_n) is less than or equal to the global average (8.09 km/s) in all parts of the study area. The lowest values (7.7–7.8 km/s) occur beneath the Junggar and Turpan-Hami basins. Beneath the Altai Mountains, Junggar Accretional Belt, Tianshan Accretional Belt, and eastern margin of the Tarim platform, P_n velocity is 8.0 km/s.

4.2. Poisson's Ratio

[31] Poisson's ratio shows the largest lateral variation within the uppermost crust (Figure 9). Poisson's ratio increases with depth in the upper crust, especially in the Mesozoic and Cenozoic basins, such as the Junggar, Turpan-Hami, and Dunhuang basins (Figure 2). We note that our measured velocities can also be affected by crustal temperatures. However, our seismic profile passes through a region of generally low surface heat flow [40–45 mW/m^2;

Table 1. The Velocity and Poisson's Ratio (σ) Structure for Different Tectonic Units

Tectonic Unit	Parameters	Uncertainty, %	Sediments	Upper Crust	Middle Crust	LV Zone	Lower Crust	Crust Thickness	km/s
Altai	H, km	5	2.12	7.60	16.00	...	729.40	56.00	7.90
	V_p, km/s	2	5.50–6.00	6.10	6.60	...	7.00		
	σ	3	0.25	0.25	0.26	...	0.28		
Junggar Basin	H, km	5	5.10	5.40	21.10	...	14.50	46.00	7.70
	V_p, km/s	2	4.3–5.8	6.10	6.50	...	6.90		
	σ	3	0.22	0.26	0.27	...	0.27		
Bogda Shan	H, km	5	3.65	10.40	16.50	...	20.30	51.00	7.70
	V_p, km/s	2	5.40–5.90	6.30	6.50	...	6.90		
	σ	3	0.25	0.25	0.26	...	0.27		
Turpan-Hami Basin	H, km	5	9.84	5.00	15.00	...	19.10	49.00	7.70
	V_p, km/s	2	3.60–5.90	6.10	6.50	...	6.90		
	σ	3	0.19	0.25	0.25	...	0.26		
Tianshan	H, km	5	2.74	9.00	12.40	7.40	18.20	50.00	7.90
	V_p, km/s	2	5.80–6.00	6.10	6.30	5.90	7.00		
	σ	3	0.25	0.25	0.25	0.25	0.27		
Tarim	H, km	5	6.07	3.00	13.00	5.30	21.70	49.00	8.00
	V_p, km/s	2	4.40–5.80	6.00	6.30	5.90	7.00		
	σ	3	0.20	0.25	0.25	0.25	0.27		

Artemieva and Mooney, 2001]. For temperatures more than 10% below the solidus, thermal effects act approximately equally for P wave and S wave velocities [*Christensen*, 1996]. Therefore we do not expect that temperature will significantly alter the measured Poisson's ratio in the upper and middle crust. The observed P_n velocity along the central portion of our profile is a low 7.7 km/s, nearly 0.4 km/s lower than the global average P_n velocity (8.09 km/s). If this low P_n velocity is due to a warm uppermost mantle, and not seismic anisotropy, we would expect that thermal effects would reduce Poisson's ratio in the uppermost mantle and lower crust. While we have not estimated Poisson's ratio in the uppermost mantle, we do observe a lower Poisson's ratio (0.26) in the central portion of the lower crust. Error estimates for Poisson's ratios are presented in Table 1.

[32] The Mesozoic and Cenozoic sedimentary basins have low values of Poisson's ratio (0.19–0.22), with the lowest value in the Turpan-Hami basin. Poisson's ratio in the upper crust is about 0.25 in most areas, except beneath the Bogda Shan, where the value is about 0.26.

[33] On the basis of Poisson's ratio, the middle crust along the transect can be divided at the Bogda Shan into a northern and southern segment. In the northern segment, including the Bogda Shan, the middle crust shows a

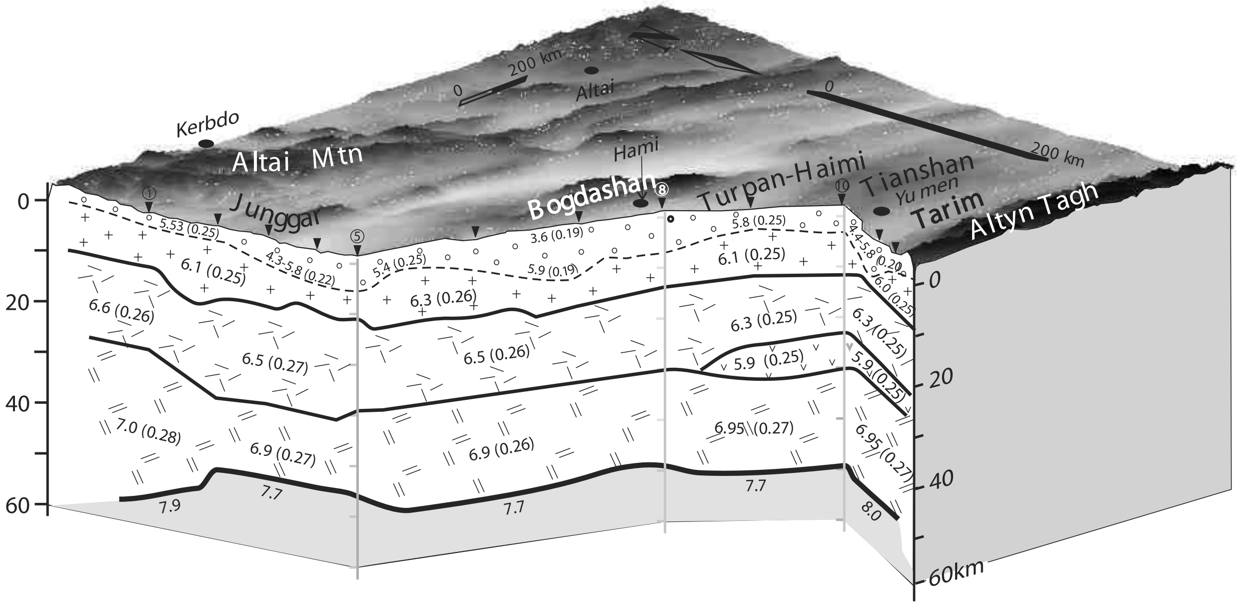

Figure 9. Three-dimensional perspective view of the crustal structure along the seismic transect from the Altai Mountains to the Altyn Tagh fault. Dashed lines indicate the top of the crystalline basement. Three distinct layers are present along this transect that we identify as the upper (6.1–6.3 km/s), middle (6.3–6.6 km/s) and lower (6.9–7.0 km/s) crust. P wave velocity values are given, as is Poisson's ratio (in parenthesis). The Moho, which is remarkably flat from the Junggar basin to the Altyn Tagh fault, is shown as a heavy, dark line.

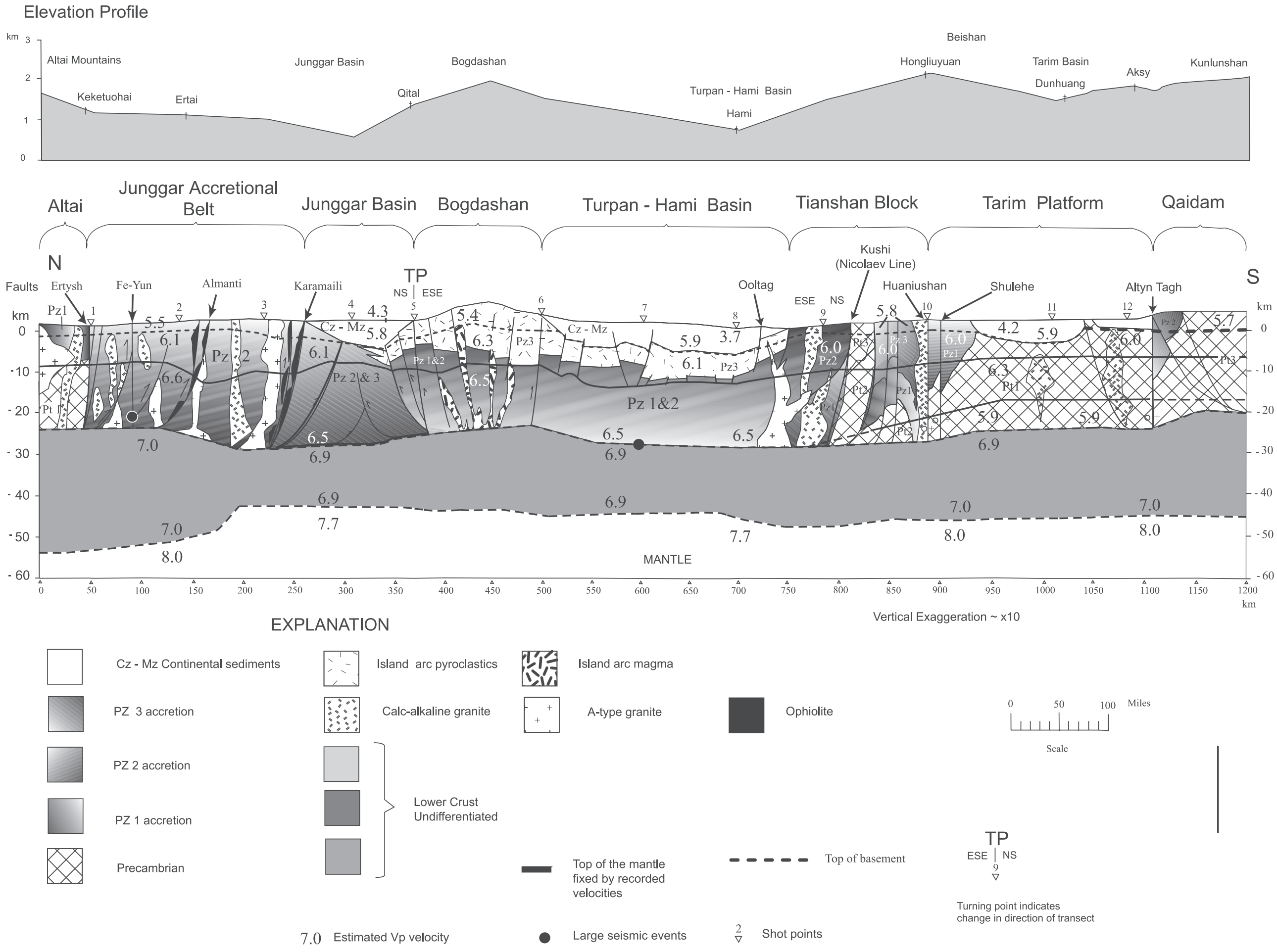

Figure 10. Geological cross section of the transect from the Altai Mountains to the Altyn Tagh fault with *P* wave velocity structure superimposed. This section follows the transect and therefore has some distortion crossing the Bogda Shan volcanic arc. The seismic transect crosses diverse crustal blocks that were accreted during the Paleozoic, but results show a relatively uniform, flat-layered, ∼50-km-thick crust (cf., Figure 9). The measured seismic velocities within the uniform, three-layered structure are taken to indicate that the crust has undergone partial melting and differentiation after the Paleozoic accretionary phase. The greater-than-average crustal thickness is interpreted as due to the subsequent Indo-Asian collision. The nonuniform composition of the accreted crustal blocks (i.e., continental and oceanic terranes, accretionary prisms, and magmatic arcs) is reflected in the variation in the measured average crustal velocity from north to south along the profile.

Poisson's ratio as high as 0.27. However, the middle crust to the south of the Bogda Shan has a more typical Poisson's ratio of around 0.25. Poisson's ratio in the lower crust is 0.26–0.28, with the highest value (0.28) beneath the Altai block, and the lowest value (0.26) beneath the Turpan-Hami basin. As discussed below, the profile segment with higher values of Poisson's ratio correlates with Nd, Sr, and Pb isotopic anomalies determined on the granitic plutons [*Hopson et al.*, 2003] indicating crust sources of oceanic (mafic) origin beneath the Junggar, Bogda Shan, and Turpan-Hami blocks. Isotopic ratios indicate that more felsic continental crust is present beneath the central and South Tianshan [*Hopson et al.*, 2003].

4.3. Geological Interpretation

[34] We have constructed a geologic cross section from the surface to the Moho along the seismic profile (Figure 10). The cross section uses information on surface geology from *Tao and Lu* [1981], *Coleman* [1989], *Yuan et al.* [1992], *Teng et al.* [1994], and *Allen and Vincent* [1999]. We describe this 1100-km-long cross section from north (Altai Mountains) to south (Altyn Tagh fault).

[35] The greatest total crustal thickness (55 km) and lower-crustal thickness (30 km) are found north of the Kelimali fault in the Altai Mountains and Junggar Accretional Belt where the high Poisson's ratio (0.28) in the lower crust is consistent with a mafic lower-crustal composition. The lower crust is less than 15 km thick beneath the Junggar basin. There has been much discussion concerning the origin of the deep basement of the Junggar basin, which may be composed of either Precambrian crystalline rocks or accreted Paleozoic metasedimentary and/or imbricated mafic oceanic rocks [*Yang and Yang*, 1981; *Tao and Lu*, 1981].

[36] In the area of the Bogda Shan Arc and Turpan-Hami basin the crustal structure inferred from geology indicates a complex evolution, and the composition and origin of the

deep crust is controversial. We correlate the high velocities and lower Poisson's ratio (0.26) with the exposed rocks that include Paleozoic ophiolitic, accretionary and arc rocks of oceanic affinity. Isotopic variations of Nd, Sr, and Pb in exposed Paleozoic granitoid plutons of this region show distinctive isotopic signatures indicative of source rocks with an oceanic affinity [*Hopson et al.*, 2003]. The crust, with these quartz-rich, postcollisional granites and abundant calc-alkaline intrusives, therefore shows evidence of homogenization and melting as a result of a late Paleozoic thermal event.

[37] Beneath the Tianshan and eastern margin of the Tarim Craton, the relatively low Poisson's ratio (0.25) and low *P* wave velocity (6.3 km/s) of the middle crust, together with an underlying LVZ (~5.9 km/s), imply the presence of abundant felsic rocks. Hence it appears that the crust in the southern part of the profile was either invaded by granitic plutons during a late Paleozoic thermal event, or that the crust has been doubled by thrusting, the LVZ being metasedimentary rocks at the top of the deeper crustal section. The lower crust (6.95 km/s) has similar values of seismic velocity and Poisson's ratio as exists to the north, and may consist of mafic granulite facies rocks. It is remarkable that the Moho is flat from the Tianshan to the Tarim basin. Thus neither the late Cenozoic uplift of the Tianshan nor the Neogene subsidence of the Tarim basin are expressed as topography on the Moho, at least along this transect.

[38] In summary, we make several inferences based on a comparison of the geophysical model and surface geology.

[39] 1. Within the Altai Mountains and its southern margin, a high-grade metamorphic Precambrian basement is indicated by high *P* and *S* wave velocities, high Poisson's ratio, and the exposure of Precambrian rocks. Maximum crustal thickening (56 km) occurs here.

[40] 2. A wide belt of accreted crust exists between the southern margin of the Junggar basin and the northern margin of the Tarim basin. The principle tectonic blocks are the Bogda Shan arc, the Turpan-Hami basin, and the Tianshan. Besides the low-velocity layer at the southern end of this transect that may reflect a midcrustal detachment surface, no other evidence has been preserved in the geometry of the deep crustal layers to record the collisional events that built this crust during the Paleozoic. Instead, the crustal layers are nearly flat-lying and rather homogeneous laterally. We suggest that this uniformity was produced by a late Paleozoic thermal event that caused the crust to undergo partial melting and differentiation. This thermal event is also evidenced by postcollisional granites and calc-alkaline intrusives. The surprisingly low Poisson's ratio (0.25–0.26) within the entire upper and middle crust is consistent with the intrusion of postcollisional, quartz-rich granites.

5. Discussion and Conclusion

5.1. Crustal Structure

[41] The depth of each of the sedimentary basins along the transect is well determined from first arrivals in the seismic data. We find that the Junggar, Turpan-Hami, and Tarim basins each have 5–10 km of sedimentary fill (Figure 10). However, we do not find any crustal thinning (i.e., Moho uplifts) beneath the sedimentary basins, as is often found elsewhere. This significant observation implies that the sedimentary basins are not the result of local crustal extension, but rather result from a combination of compressional and especially horizontal (strike-slip) deformation.

[42] The crystalline crust consists of an upper, middle, and lower crust with seismic velocities of 6.0–6.3, 6.3–6.6, and 6.9–7.0 km/s, respectively. Several important features are evident along the transect. (1) The Bogda Shan arc shows the highest upper crustal velocities (6.3 km/s), indicative of higher densities due to the uplift of midcrustal rocks. (2) The seismic velocities within the middle-crustal layer are 6.5–6.6 km/s from the Altai Mountains to the Turpan-Hami basin, and then decrease to 6.3 km/s beneath the Tianshan and the Tarim basin (Figure 9). Thus the northern boundary of the Tianshan marks a fundamental change in crustal structure, with a more dense and mafic crust to the north and a lower-density, silicic crust to the south. (3) Beneath the Tianshan and continuing to the south, a 5-km-thick LVZ (5.9 km/s) in the middle crust is found at 25–30 km depth. This LVZ may serve as a detachment surface upon which the upper crust of the Tianshan and Tarim basin are thrust, or may be a zone of silicic igneous intrusions. (4) The high-velocity (6.9–7.0 km/s) lower-crustal layer has an average thickness of 20 km along the entire profile. It reaches a maximum thickness of 30 km beneath the southern margin of the Altai Mountains and a minimum thickness of 15 km beneath the Junggar basin. Both the higher seismic velocities throughout the crust and isotopic ratios (Nd, Sr, Pb) from the granitic plutons [*Hopson et al.*, 2003], indicate the presence of oceanic crust and mantle north of the Tianshan, i.e., beneath the Junggar, Bogda Shan, and the Turpan-Hami blocks (Figure 10), and felsic continental crust beneath the central and South Tianshan. (5) The seismic velocity of the uppermost mantle (P_n) is a low 7.7 km/s, except beneath the Altai Mountains to the north and the Tarim basin to the south. This P_n velocity is ~0.4 km/s lower than the global average (8.09 km/s) and indicated either significant seismic anisotropy or elevated temperatures in the uppermost mantle. Surface heat flow is low (40–45 mW/m^2) which indicates that seismic anisotropy is the more likely explanation.

[43] The three-layer stratification of the crust into well-defined upper, middle, and lower crust on this profile is similar to stable continental crust elsewhere (i.e., Precambrian platforms and shields). However, the lower-crustal layer (6.9–7.0 km/s) is remarkably thick, with an average thickness of 20 km (amounting to some 40% of the total crustal thickness). The middle crust (6.3–6.6 km/s) has an average thickness of 17 km, but the upper (crystalline) crust has an average thickness of only 9 km. Sedimentary accumulations range from 0 to 10 km in thickness. The average thickness of the entire crust along the profile is 50 km, and the middle and lower crust comprise 74% of the crust.

5.2. Crustal Thickening

[44] The crustal thickness (~50 km) found in this study is 11 km thicker than the global average for continental crust [39 km; *Christensen and Mooney*, 1995]. Crustal thickening is likely to be the result of compressional shortening associated with the Tibetan orogeny and/or magmatic additions. In order to thicken a 39-km-thick crust to a net thickness of 50 km, 30% shortening is required. However, the fact that the upper crust (6.0–6.3 km/s) has only

approximately half the thickness of the middle and lower crust suggests that isostatic uplift has caused erosion of about 10 km of the (shortened) upper crust. If we tentatively accept that 10 km of crust has been removed, then the shortening along the profile amounts to 50%. A major uncertainty in this calculation is the initial crustal thickness.

[45] Alternatively, the crust may have been thickened by magmatic additions. If magmatism was mainly of intermediate to mafic composition, thickening will have occurred mainly in the middle and lower crust. Silicic intrusions may have thickened the upper crust, which was subsequently thinned by erosion processes. The present geophysical data do not allow us to discern which process, compression or magmatic addition, has dominated the mechanism of crustal thickening.

5.3. Crustal Composition

[46] The interpretation of crustal composition from seismic velocity measurements has recently been reviewed by *Holbrook et al.* [1992], *Rudnick and Fountain* [1995], and *Christensen and Mooney* [1995]. We begin our discussion with the measured V_p structure, and then proceed to the V_p/V_s ratio, or equivalently, Poisson's ratio.

[47] The average *P* wave velocity of the crystalline crust varies along the seismic transect, with important boundaries coinciding with: (1) the southern Junggar Accretional Belt and (2) the northern Tianshan. Beneath the Altai Mountains and the Junggar Accretional Belt (SP1 and SP2; Figure 10) the average crustal velocity is 6.7 km/s. This value, which is significantly higher than the global average (6.45 km/s), is due to two factors: (1) the moderately high seismic velocity (6.5–6.6 km/s) of the middle crust and (2) the unusually large thickness (30 km) of the high-velocity (7.0 km/s) lower crust (Figure 10). Between the Junggar basin and the northern flank of the Tianshan (SP3 through SP8; Figure 10) the average crustal velocity is 6.5 km/s, a value that is essentially equal to the global average. From the Tianshan to the Altyn Tagh fault, the average crustal velocity is 6.3 km/s, a value that is 0.15 km/s lower than the global average and is significantly lower (0.2–0.4 km/s) than the portion of the transect north of the Tianshan. Thus three crustal types may be clearly distinguished along this transect on the basis of average crustal velocities of 6.3, 6.5, and 6.7 km/s. The origin of these crustal types may be attributed to: (1) diverse accreted terranes (magmatic arcs, oceanic crust, continental fragments) that form the crust and (2) different amounts of crustal shortening and postaccretional magmatic additions that have modified the crust.

[48] *Christensen and Mooney* [1995] present statistical averages of seismic velocity as a function of depth for continental crust, and relate seismic velocity to rock types. Upper crustal velocities in the study area are consistent with geologically observed metasedimentary and felsic intrusive rocks. Measured Poisson's ratio for these rocks (0.25) are consistent with this interpretation. As noted above, seismic velocities within the middle crust are lower beneath the Tianshan and eastern Tarim basin (V_p = 6.3 km/s) than under the terranes to the north (V_p = 6.5–6.6 km/s), and Poisson's ratio increases slightly from south (0.25) to north (0.26–0.27). These observations indicate that the bulk composition of middle crust beneath the Tianshan is close to that of a tonalite or granodiorite, and becomes more mafic to the north (i.e., equivalent to a diorite). For example, an increase in the abundance of amphibolite in the middle crust from 5% beneath the Tianshan to about 35% beneath the terranes to the north would satisfy the observations [cf., Figure 18 of *Christensen and Mooney*, 1995]. The seismic velocity (6.9–7.0 km/s) and Poisson's ratio (0.26–0.28) of the lower crust are remarkably uniform along the entire 1100 km transect. The seismic measurements are consistent with a mafic composition (mafic granulite and/or mafic garnet-granulite), or anorthosite (less likely). *Hopson et al.* [2003] suggested that the lower crust consists largely of mafic migmatite in which a large mafic (amphibolite and granulite) and ultramafic (meta peridotite) component is responsible for the 6.9–7.0 km/s *P* wave velocity, whereas a subordinate granitoid (i.e., metadiorite, metatonalite, and leucotrondhjemite) component is responsible for a somewhat lower-than-expected Poisson's ratio. However, these compositions could provide a Poisson's ratio as high as 0.29–0.31, which is 0.01–0.05 higher than the measured values. Granulite grade metapelite provides the best fit to the seismic velocity data, but it seems unlikely, based on heat flow constraints and volumetric considerations, that the lower continental crust is composed of a thick (20 km) layer of metapelite over a distance of 1100 km. Thus we favor mafic granulite composition.

[49] Our crustal cross section (Figure 10), which is based on surface geology and *P* and *S* wave seismic velocities, reveals a 50-km-thick crust that is remarkable for its relatively uniform three-layer stratification. The crustal structure (layer velocities, thickness, and Poisson's ratio) of the central portion of the profile (i.e., from the Turpan-Hami basin to the Junggar basin) is similar to that of Precambrian platforms and shields [*Rudnick and Fountain*, 1995; *Christensen and Mooney*, 1995]. We therefore conclude that the accretionary process combined with compression and ~50% crustal shortening, with some magmatic additions to the base of the crust, is a valid description of the formation and evolution of stable continental crust. The outstanding major question in this study area is the composition and configuration of the underlying mantle lithosphere. Such information can be obtained from geochemical studies and seismological investigations that probe to sub-Moho depths.

[50] **Acknowledgments.** The first and third authors would like to express their appreciation for the support of the scientific exchange program of the U.S. Geological Survey. We thank those who provided advice on the data processing and interpretation during this research, including G.A. Thompson from Stanford University, USA; C. Prodehl and F. Wenzel from the Geophysical Institute at Karlsruhe, Germany; G. Fuis, J.H. Luetgert and J. Hole from the U.S. Geological Survey; T. Ohminato from the Japan Geological Survey; E. Gurria from Intituto Geografico Nacional, Spain. We thank J. Hole for providing the data analysis code of the finite difference travel time inversion and T. Ohminato for using his finite difference algorithm for 2-D heterogeneous media with transparent boundary conditions and topography to calculate the synthetic seismograms in this research. The Stanford China Industrial Group provided much new data concerning basin development and C.A. Hopson has shared new isotopic data on granites closely related to the transect. Review comments from R. Girdler, K. Favret, G. Chulick, S. Detweiler, R. Meissner and Y. Laursen, P.R. Reddy, S. van der Lee, K. Vogfjord, and an anonymous reviewer greatly improved the manuscript.

References

Allen, M. B., and S. J. Vincent, Late Cenozoic tectonics of the Kepinstage thrust zone: Interactions of the Tianshan and Tarim basin, northern China, *Tectonics*, *18*, 639–654, 1999.

Allen, M. B., B. F. Windley, C. Zhang, Z. Zhao, and G. Wang, Basin evolution within and adjacent to the Tien Shan range, NW China, *J. Geol. Soc. London*, *148*, 369–378, 1991.

Allen, M. B., B. F. Windley, and C. Zhang, Cenozoic tectonics in the Urumqi-Korla region of the Chinese Tien Shan, *Geol. Rundsch.*, *83*, 406–416, 1992.

Allen, M. B., B. F. Windley, and C. Zhang, Paleozoic collisional tectonics and magmatism of the Chinese Tien Shan, central Asia, *Tectonophysics*, *220*, 89–115, 1993.

Allen, M. B., M. C. Sengor, and B. A. Natal'in, Junggar, Turfan and Alakol basins as Late Permian to Early Triassic extensional structures in a sinistral shear zone in the Altaid orogenic collage, central Asia, *J. Geol. Soc. London*, *152*, 327–338, 1995.

Artemieva, I. M., and W. D. Mooney, Thermal thickness and evolution of Precambrian lithosphere: A global study, *J. Geophys. Res.*, *106*, 16,387–16,414, 2001.

Avouac, J.-P., and P. Tapponnier, Kinematic model of active deformation in central Asia, *Geophys. Res. Lett.*, *20*, 895–898, 1993.

Avouac, J.-P., P. Tapponnier, M. Bai, H. You, and G. Wang, Active thrusting and folding along the Tien Shan and late Cenozoic rotation of the Tarim relative to Dungaria and Kazakhstan, *J. Geophys. Res.*, *98*, 6755–6804, 1993.

Berzin, N. A., R. G. Coleman, N. L. Dobretsov, L. P. Zonenshain, X. Xiao, and E. Z. Chang, Geodynamic map of the western part of the Paleoasian Ocean, *Russ. Geol. Geophys.*, *35*(7–8), 5–22, 1994.

Bibkova, Y. V., T. I. Kimozova, I. K. Kozakov, A. B. Kotav, L. A. Neymark, B. M. Gorokhovskiy, and I. K. Shuleshko, U-Pb ages for polymetamorphic complexes on the southern flank of the Mongolian and Gobi Altai, *Geotectonics*, *26*, 166–172, 1992.

Burov, E. V., M. G. Kogan, H. Lyon-Caen, and P. Molnar, Gravity anomalies, the deep structure, and dynamic processes beneath the Tian Shan, *Earth Planet. Sci. Lett.*, *96*, 367–383, 1990.

Carroll, A. R., S. A. Graham, S. A. Hendrix, J. Chu, C. L. McKnight, X. Xiao, and Y. Liang, Junggar basin, northwest China: Trapped late Paleozoic ocean, *Tectonophysics*, *181*, 1–14, 1990.

Carroll, A. R., S. A. Graham, M. S. Hedrix, D. Ying, and D. Zhou, Late Paleozoic tectonic amalgamation of northwestern China: Sedimentary record of the northern Tarim, northwest Turpan, and southern Junggar basins, *Geol. Soc. Am. Bull.*, *107*, 571–594, 1995.

Castagna, J. P., Relationships between compressional wave and shear wave velocity in clastic silicate rocks, *Geophysics*, *50*(4), 571–581, 1985.

Catchings, R. D., Regional V_p, V_s, V_p/V_s, and Poisson's ratios across earthquake source zones from Memphis, Tennessee, to St. Louis, Missouri, *Bull. Seismol. Soc. Am.*, *89*, 1591–1605, 1999.

Catchings, R. D., and W. H. K. Lee, Shallow velocity structure and Poisson's ratio at the Tarzana, California, strong-motion accelerometer site, *Bull. Seismol. Soc. Am.*, *86*, 1704–1713, 1996.

Cerveny, V., and I. Psencik (Eds.), SEIS83-numerical modeling of seismic wavefield in 2-D laterally varying layered structures by the ray method, in *Documentation of Earthquake Algorithms*, edited by E. R. Engdahl, *Rep. SE-35*, pp. 36–40, World Data Cent. (A) for Solid Earth Geophys., Boulder, Colo., 1984.

Cerveny, V., I. A. Molotkov, and I. Psencik, *Ray Method in Seismology*, pp. 57–158, Univ. Karlova, Prague, 1977.

Chen, W.-P., C.-Y. Chen, and J. L. Nábelek, Present-day deformation of the Qaidam basin with implications for intra-continental tectonics, *Tectonophysics*, *305*, 165–181, 1999.

Christensen, N. I., Poisson's ratio and crustal seismology, *J. Geophys. Res.*, *101*, 3139–3156, 1996.

Christensen, N. I., and W. D. Mooney, Seismic velocity structure and composition of the continental crust: A global view, *J. Geophys. Res.*, *100*, 9761–9788, 1995.

Coleman, R. G., Continental growth of northwest China, *Tectonics*, *8*, 621–635, 1989.

Cotton, F., and J.-P. Avouac, Crustal and upper mantle structure under the Tien Shan from surface wave dispersion, *Phys. Earth Planet. Inter.*, *84*, 95–109, 1994.

Cunningham, W. D., B. F. Windley, D. Dorjnamjaa, J. Badamgarov, and M. Saandar, Late Cenozoic transpression in southwestern Mongolia and the Gobi Altai-Tien Shan connection, *Earth Planet. Sci. Lett.*, *140*, 67–81, 1996a.

Cunningham, W. D., B. F. Windley, D. Dorjnamjna, G. Badamgarov, and M. Saandar, A structural transect across the Mongolian Western Altai; active transpressional mountain building in central Asia, *Tectonics*, *15*, 142–156, 1996b.

Dong, S., Metamorphic and tectonic domains of China, *J. Metamorph. Geol.*, *11*, 465–481, 1993.

Eberhart-Phillips, D., and A. J. Michael, Seismotectonics of the Loma Prieta, California, region determined from three-dimensional V_p, V_p/V_s, and seismicity, *J. Geophys. Res.*, *103*, 21,099–21,120, 1998.

Eesley, R. A., Analysis of compressional and shear-wave seismic data from the Prudhoe Bay Field, *Leading Edge*, *11*, 10–13, 1989.

Feng, R., J. S. Zhu, Y. Y. Ding, G. Y. Chen, Z. Q. He, S. B. Xiang, H. N. Zhou, and K. Z. Shun, Using surface wave to study the crust structure of China, *Acta Seismol. Sin.*, *3*, 335–350, 1980.

Feng, Y., R. G. Coleman, G. Tilton, and X. Xiao, Tectonic evolution of the W. Junggar Region, Xinjiang, China, *Tectonics*, *8*, 729–752, 1989.

Fuchs, K., and G. Müller, Computation of synthetic seismograms with the reflectivity method and comparison with observations, *Geophys. J. R. Astron. Soc.*, *23*, 417–433, 1971.

Gajewski, D., R. Stangle, K. Fuchs, and K. J. Sandmeier, A new constraint on the composition of the topmost continental mantle—Anomalously different depth increases of *P*- and *S*-wave velocity, *Geophys. J. Int.*, *103*, 497–507, 1990.

Giese, P., C. Prodehl, and A. Stein, *Explosion Seismology in Central Europe*, pp. 146–161, Springer-Verlag, New York, 1976.

Greene, T. J., A. R. Carroll, M. S. Hendrix, J. Chu, and C. L. McKnight, Permian-Triassic basin evolution and petroleum system of the Turpan-Hami basin, Xinjiang Province, northwest China, in *Annual Meeting Abstracts*, vol. 6, p. 42, Am. Assoc. of Pet. Geol., Tulsa, Okla., 1997.

Hauksson, E., and J. S. Haae, Three-dimensional V_p and V_s velocity models of the Los Angeles basin and central transverse ranges California, *J. Geophys. Res.*, *102*, 5423–5453, 1997.

Hawman, R. B., Wide-angle, three-component seismic reflection profiling of the crust along the East Coast Gravity High, southern Appalachians, using quarry blasts, *J. Geophys. Res.*, *101*, 13,933–13,945, 1996.

Hendrix, M. S., T. A. Dumitru, and S. A. Graham, Late oligocene-early miocene unroofing in the Chinese Tian Shan: An early effect of the India-Asia collision, *Geology*, *22*, 487–490, 1994.

Holbrook, W. S., D. Gajewski, A. Krammer, and C. Prodehl, An interpretation of wide-angle compressional and shear wave data in Southwest Germany: Poisson's ratio and petrological implications, *J. Geophys. Res.*, *93*, 12,081–12,106, 1988.

Holbrook, W. S., W. D. Mooney, and N. I. Christensen, The seismic velocity structure of the deep continental crust, in *Continental Lower Crust*, edited by D. M. Fountain, R. Arculus, and R. W. Kay, pp. 1–43, Elsevier Sci., New York, 1992.

Hole, J. A., Nonlinear high-resolution three-dimensional seismic travel time tomography, *J. Geophys. Res.*, *97*, 6553–6562, 1992.

Hopson, C. A., J. Wen, Y. Tang, and G. R. Tilton, Geology and isotopic variation of Nd, Sr, and Pb in Paleozoic granitoid plutons along an East Junggar-Bogda Shan-Tianshan transect, NW China, with tectonic implications, *Int. Geol. Rev.*, in press, 2003.

Jia, C., H. Yao, G. Wei, and L. Wei, Plate tectonic evolution and characteristics of major tectonics units of the Tarim basin, in *The Tarim Basin*, edited by X. Tong and D. Liang, pp. 207–225, Xinjiang Sci., Urumqi, China, 1991.

Kao, H., R. Gao, R.-J. Rau, D. Shi, R.-Y. Chen, Y. Guan, and F. Wu, Seismic image of the Tarim basin and its collision with Tibet, *Geology*, *29*, 575–578, 2001.

Kelly, K. R., R. W. Ward, S. Treitel, and R. M. Alford, Synthetic seismograms: A finite-difference approach, *Geophysics*, *41*, 2–27, 1976.

Kern, H., S. Gao, Z. Jin, T. Popp, and S. Jin, Petrophysical studies on rocks from the Dabie ultrahigh-pressure (UHP) metamorphic belt, central China: Implications for the composition and delamination of the lower crust, *Tectonophysics*, *301*, 191–215, 1999.

Kosminskaya, I. P., Progress in deep seismic sounding studies of the Earth's crust and upper mantle, in *1993, CCSS Workshop Proceedings Volume*, edited by W. D. Mooney, pp. 165–194, U.S. Geol. Surv., Menlo Park, Calif., 1995.

Krilov, S. V., V. S. Mishenkina, V. S. Seleznjov, and I. F. Sheludko, Methods and results of detailed seismic investigations of the Earth's crust in the Baikal rift zone, in *CCSS Workshop Proceedings*, edited by W. D. Mooney, pp. 9–33, U.S. Geol. Surv., Menlo Park, Calif., 1995.

Kwon, S. T., G. R. Tilton, R. G. Coleman, and Y. Feng, Isotopic studies bearing on the tectonics of the west Junggar region, Xiangiang, China, *Tectonics*, *8*, 753–757, 1989.

Liu, F., K. X. Qu, H. Wu, Q. Li, J. Hua, and G. Hu, The tomography of Chinese Continent and its adjacent area, *Acta Geophys. Sin.*, *32*, 281–291, 1989.

Liu, H., H. Liang, L. Cai, Y. Xia, and L. Liu, Evolution and structure style of Tianshan and adjacent basins, northwestern China, *J. China Univ. Geosci.*, *5*, 46–54, 1994.

Mahdi, H., and G. L. Pavlis, Velocity variations in the crust and upper mantle beneath the Tien Shan inferred from Rayleigh wave dispersion: Implications for tectonic and dynamic processes, *J. Geophys. Res.*, *103*, 2693–2703, 1998.

Menke, W., M. West, B. Brandsdottir, and D. Sparks, Compressional and shear velocity structure of the lithosphere in Northern Iceland, *Bull. Seismol. Soc. Am.*, *86*, 1561–1571, 1998.

Molnar, P., and P. Tapponnier, Cenozoic tectonics of Asia: Effects of a continental collision, *Science*, *189*, 419–426, 1975.
Musacchio, G., W. D. Mooney, J. H. Luetgert, and N. I. Christensen, Composition of the crust in the Grenville and Appalachian Provinces of North America inferred from V_p/V_s ratios, *J. Geophys. Res.*, *102*, 15,225–15,241, 1997.
Neil, E. A., and G. A. Houseman, Geodynamics of the Tarim basin and the Tianshan in central Asia, *Tectonics*, *16*, 571–584, 1997.
Ohminato, T., and B. Chouet, A free-surface boundary condition for including 3D topography in the finite difference method, *Bull. Seismol. Soc. Am.*, *87*, 494–515, 1997.
Qu, G., and G. He, The orogeny in the Altaides, *Acta Geol. Sin.*, *6*(1), 1–5, 1993.
Ren, J., C. Jiang, Z. Zhang, D. Qin, and T. K. Huang, *Geotectonic Evolution of China*, pp. 56–68, Science, Enfield, N. H., 1987.
Ritts, B. D., Mesozoic tectonics of the Qaidam region, NW China, and the relationship between Mesozoic Qaidam and Tarim basins (abstracts with Programs 1995 Annual Meeting), *Geol. Soc. Am.*, *27*(6), 456, 1995.
Ritts, B. D., and U. Biffi, Magnitude of post-Middle Jurassic (Bajocian) displacement on the Altyn Tagh fault system, northwest China, *Geol. Soc. Am. Bull.*, *112*, 61–74, 2000.
Roecker, S. W., T. M. Sabitova, L. P. Vinnik, Y. A. Burmakov, M. I. Golvanov, R. Mamatkanova, and L. Munirova, Three-dimensional elastic wave velocity structure of the western and central Tianshan, *J. Geophys. Res.*, *98*, 15,779–15,795, 1993.
Romero, A. E., Jr., T. V. McEvilly, and E. L. Majer, Velocity structure of the Long Valley Caldera from the inversion of local earthquake *P* and S travel times, *J. Geophys. Res.*, *98*, 19,869–19,879, 1993.
Rowly, D. B., Age of initiation of collision between India and Asia: A review of stratigraphic data, *Earth Planet. Sci. Lett.*, *145*, 1–13, 1996.
Rudnick, R. L., and D. M. Fountain, Nature and composition of the continental crust: A lower crustal perspective, *Rev. Geophys.*, *33*(3), 267–309, 1995.
Sengor, A. M. C., B. A. Natalin, and V. S. Burtman, Evolution of the Altaid tectonic collage and Palaeozoic crustal growth in Eurasia, *Nature*, *364*, 299–307, 1993.
Sobel, E. R., Basin analysis of the Jurassic-Lower Cretaceous southwest Tarim basin, northwest China, *Geol. Soc. Am. Bull.*, *111*, 709–724, 1999.
Song, Y., S. Wang, and D. Fang, The formation and development of petroleum systems in Junggar Basin, Xinjiang, China, *Acta Petrol. Sin.*, *21*, 20–25, 2000.
Stoerzel, A., and S. B. Smithson, Two-dimensional travel time inversion for the crustal *P*- and *S*- wave velocity structure of Ruby Mountains metamorphic core complex, N E Nevada, *J. Geophys. Res.*, *103*, 21,121–21,143, 1998.
Swenson, J. L., S. L. Beck, and G. Zandt, Crustal structure of the Altiplano from broadband regional waveform modeling: Implications for the composition of thick continental crust, *J. Geophys. Res.*, *105*, 607–621, 2000.
Tao, J., and Z. Lu, The preliminary research on plate tectonics in Xingjiang area, *Xingjiang Geol.*, *1*, 10–17, 1981.
Tapponnier, P., G. Peltzer, A. Y. Le Dain, R. Armijo, and P. Cobbold, Propagating extrusion tectonics in Asia, *Geology*, *10*, 611–616, 1982.
Tapponnier, P., Z. Xu, F. Roger, B. Meyer, N. Arnaud, G. Wittlinger, and J. Yang, Oblique stepwise rise and growth of the Tibet Plateau, *Science*, *294*, 1671–1677, 2001.
Teng, J. W., H. Wu, A. Wang, and X. Sun, The lithosphere structure and dynamics of south China and its continental margin, paper presented at the 29th International Geological Congress, Kyoto, Japan, vol. 2, p. 427, 1992.
Teng, J. W., F. T. Liu, Y. Quan, J. Liu, Y. Liu, J. Wei, L. Ji, and Z. Yang, Seismic tomography of the crust and mantle under the orogenic belts and sedimentary basins of Northwestern China, *Adv. Solid Earth Geophys. China*, *1*, 6–80, 1994.
Wang, Y. X., Discussion on division problem of tectonic units in Xinjiang area from seismic refraction results, paper presented at the 29th International Geological Congress, vol. 2, p. 463, 1992.
Wang, Y. X., X. Z. Xu, and G. H. Han, Studies on 2-D crustal velocity structure along V9-3 wide-angle reflection profile of geoscience transect from Taiwan to Altai (Chinese), in *Memoirs of the Geoscience Transection for the Continental Lithosphere Beneath Altai-Taiwan, China*, edited by X. C. Yuan, pp. 14–20, China Univ. of Geosci. Press, Wuhan, China, 1997.
Windley, B. F., M. B. Allen, C. Zhang, Z. Zhao, and G. Wang, Paleozoic accretion and Cenozoic redeformation of Chinese Tien Shan range, central Asia, *Geology*, *18*, 128–131, 1990.
Windley, B. F., J. Guo, J. Li, and C. Zhang, Subdivisions and tectonic evolution of the Chinese Altai, *Russ. Geol. Geophys.*, *35*(7–8), 98–99, 1994.
Xu, X. Z., and Y. X. Wang, The velocity characteristics of geoscience transect from Keketuohai to Aksai, paper presented at PROJECT 283: Geodynamic Evolution and Main Sutures of Paleoasian Ocean, Beijing, China, 1991.
Yang, S. N., and W. R. Yang, *Regional Tectonics of China*, Geol Publ. House, Beijing, China, 1981.
Yin, A., and S. Nie, A Phanerozoic palinspastic reconstructions of China and its neighboring regions, in *Tectonic Evolution of Asia*, edited by A. Yin and T. M. Harrison, pp. 442–485, Cambridge Univ. Press, New York, 1996.
Yin, A., S. Nie, P. Craig, and T. M. Harrison, Late Cenozoic tectonic evolution of the southern Chinese Tianshan, *Tectonics*, *17*, 1–27, 1998.
Yuan, X., Y. Zuo, and C. Zhnag, Evidences for the West China Craton and its evolution, in *Proceedings of the Twenty Ninth International Geological Conference, Kyoto, Japan*, edited by R. G. Coleman, VSP, Utrecht, 1992.
Zandt, G., and C. J. Ammon, Continental crust composition constrained by measurements of crustal Poisson's ratio, *Nature*, *374*, 152–154, 1995.
Zandt, G., A. Velasco, and S. L. Beck, Composition and thickness of the southern Altiplano crust, Bolivia, *Geology*, *22*, 1003–1006, 1994.
Zhang, C. W., Basic tectonic framwork and evolution of Altai-Altun region, in *Memoirs of the Geoscience Transection for the Continental Lithosphere Beneath Altai-Taiwan*, China, edited by Y. Xuecheng, China Univ. of Geosci. Press, Wuhan, China, 1997.
Zhang, Z., J. Liou, and R. G. Coleman, An outline of plate tectonics of China, *Geol. Soc. Am. Bull.*, *95*(3), 295–312, 1984.
Zhou, D., and S. A. Graham, Extrusion of the Altyn Tagh wedge: A kinematic model for the Altyn Tagh fault and palinspastic reconstruction of northern China, *Geology*, *24*, 427–430, 1996.

R. G. Coleman, Department of Geology and Environmental Sciences, Stanford University, Stanford, CA 94305, USA.
W. D. Mooney, U.S. Geological Survey, 345 Middlefield Road, MS 977, Menlo Park, CA 94025, USA. (mooney@usgs.gov)
Y. Wang, Department of Resources and Environmental Engineering, Guilin Institute of Technology, Guilin 541004, China.
X. Yuan, China Geological Survey, 31 Xueyuan Lu, Beijing, 100081, China.